

# GS-2DGS: Geometrically Supervised 2DGS for Reflective Object Reconstruction

Jinguang Tong<sup>1,2</sup>, Xuesong Li<sup>1,2</sup>, Fahira Afzal Maken<sup>2</sup>, Sundaram Muthu<sup>2,3</sup>  
Lars Petersson<sup>2</sup>, Chuong Nguyen<sup>1,2</sup>, Hongdong Li<sup>1</sup>

<sup>1</sup>Australian National University <sup>2</sup>CSIRO <sup>3</sup>Indian Institute of Technology Madras

## Abstract

*3D modeling of highly reflective objects remains challenging due to strong view-dependent appearances. While previous SDF-based methods can recover high-quality meshes, they are often time-consuming and tend to produce over-smoothed surfaces. In contrast, 3D Gaussian Splatting (3DGS) offers the advantage of high speed and detailed real-time rendering, but extracting surfaces from the Gaussians can be noisy due to the lack of geometric constraints. To bridge the gap between these approaches, we propose a novel reconstruction method called GS-2DGS for reflective objects based on 2D Gaussian Splatting (2DGS). Our approach combines the rapid rendering capabilities of Gaussian Splatting with additional geometric information from foundation models. Experimental results on synthetic and real datasets demonstrate that our method significantly outperforms Gaussian-based techniques in terms of reconstruction and relighting and achieves performance comparable to SDF-based methods while being an order of magnitude faster. Code is available at <https://github.com/hirotong/GS2DGS>*

## 1. Introduction

Modeling 3D assets of specular objects from multi-view images has been a long-standing and challenging task in computer graphics and vision, since specular reflections are view-dependent and thus violate the multi-view consistency assumption adopted by most reconstruction methods. Previous works [28, 32] achieve promising results by using a neural radiance field (NeRF) and a signed distance field (SDF). However, these methods require a significant computing effort to train, sometimes hours for a single scene.

The difficulty of reconstructing reflective objects lies in the ill-posed nature of the problem. The appearance of a reflective surface is determined by a combination of the surface properties (material and geometry) and the lighting condition of the environment [23], while previous methods [28, 32] consider only one of these factors.

Since 3D Gaussian Splatting (3DGS) [26] achieves sig-

nificantly higher rendering speed with greater detail and photo consistency, it has been widely used in 3D scene modeling. However, the surface reconstruction of 3DGS needs further improvement. On the one hand, several Gaussian-based methods [10, 20, 50] attempt to improve reconstruction quality by imposing additional constraints on the surface geometry by flattening the Gaussians or incorporating SDF for additional smoothness. Such approaches achieve superior reconstruction quality on common multi-view images with a much improved computational efficiency. On the other hand, some other works [18, 22, 31] address the rendering performance and enable relighting of Gaussian-based methods by introducing physical-based rendering and inverse rendering (IR) techniques. It should be noted, however, that these methods still have limitations in reconstructing reflective objects as they only consider one aspect of the problem.

A naive approach of simply combining these two aspects is not enough to address the issue of reflective object reconstruction, because of the ill-posed nature of the problem. To this end, a straightforward approach is to include additional constraints either on the properties of the surface or the lighting condition. Recent works [3, 16, 25, 34] based on transformer or diffusion models and trained with a large amount of real and synthetic data have shown impressive performance on monocular geometry (depth and normal) estimation. Unlike multiview stereo methods, which infer geometry information from multiview consistency, these methods directly predict geometry from a single view based on the knowledge of massive training data, thus making them unsusceptible to the reflective surface problem.

In this paper, we propose a novel framework for modeling reflective object reconstruction by leveraging foundation models in physical-based Gaussian splatting. By incorporating additional information on the surface, our method can simultaneously address the issues arising from both surface-related properties (geometry and material) and lighting conditions. Our method is achieving state-of-the-art results by some margin with respect to Gaussian Splatting based methods, and it is achieving results on par with NeRF-based methods while being an order of magnitude

faster.

To summarize, our contributions are as follows:

- We propose a novel framework for reflective object reconstruction by leveraging foundation models in physical-based Gaussian splatting.
- We introduce the deferred shading technique to improve the estimation of environmental lighting.
- We achieve state-of-the-art results on reflective object reconstruction by addressing both surface-related properties and lighting conditions.

## 2. Related work

### 2.1. Radiance field for geometry reconstruction

Neural reconstruction methods can be divided into the following categories: Neural Radiance Fields (NeRF), Signed Distance Fields (SDF) and Gaussian Splatting (GS). First, NeRF [35] is well known as a pioneering approach for novel view synthesis of complex scenes based on Multi-Layer Perception (MLP). Variants of NeRF include Mip-NeRF [2] for antialiasing, Plenotrees [49] for fast rendering, and Instant NeRF [53] for fast reconstruction. Second, SDF approach is popularized by NeuS [53] where an MLP is used to encode SDF to model the 3D surface of the scene. Recent SDF approaches include NeuS2[45] for fast neural surface reconstruction using multi-resolution hash encodings, Neuralangelo [30] for using higher-order derivatives supervision. Finally, GS was recently proposed by [26] as a fast and high photo consistency alternative for neural rendering. Further extensions include 2DGS [20] for using 2D Gaussians instead of 3D Gaussian, PGSR [6] for flattening 3D Gaussians along their smallest axis, and GSDF [50] for combining the best of SDF and GS.

### 2.2. Reflective object reconstruction

Reconstructing highly reflective objects is challenging and requires special treatment [19, 21, 41, 42]. Traditional approaches for reconstructing transparent and reflective objects as reported by [21] require deep knowledge of optical phenomena and physical modeling that treat specific cases separately. Recent neural radiance-based approaches allow a range of complex optical phenomena and larger scenes to be modeled more effectively.

NeRF-based approaches such as NeRFReN [19] model the reflection by including a second MLP branch, while Ref-NeRF [42] replaces NeRF’s view dependence with Integrated Directional Encoding, and Planar Reflection-Aware NeRF [17] identifies and models planar reflectors as a ray tracing problem.

For SDF-based approaches, NeRO [32] includes a novel light representation based on slit-sum approximation for highly reflective objects, while TensorSDF [28] employs a surface roughness-aware tensorial representation.

For GS approaches, R3DG [18] proposes point-based ray-tracing to improve the relighting quality of reflective objects, while GS-IR [31] and GaussianShader [22] focus on incorporating inverse rendering and simplified approximation of the rendering equation, respectively.

### 2.3. Monocular depth/normal estimation

Monocular depth estimation involves predicting depth from a single RGB image [15, 39], a task that has progressed from multi-scale networks [14] to advanced approaches like transformers [38, 46, 51] and diffusion models [33, 40]. Methods such as MiDaS [37] and MegaDepth [29] leverage large-scale datasets to achieve affine-invariant depth predictions, which generalize well to unseen scenes but remain ambiguous in scale and shift, limiting their applicability for metric depth estimation. Diffusion-based models, including DiffusionDepth [12] and VPD [52], have further improved cross-domain generalization by leveraging pre-trained latent diffusion models. However, these methods often require fine-tuning or additional inputs, such as camera intrinsics, making them computationally demanding.

Surface normal estimation [52], on the other hand, captures local geometric details without metric ambiguities, making it valuable for tasks like scene reconstruction and object localization. Methods like GeoNet [48] and DSINE [1] enhance generalization by enforcing depth-normal consistency and leveraging diverse datasets, while OmniData [13] provides large-scale annotated normals for improved training. These approaches aim to improve generalization, sharpen occlusion boundaries, and reduce dependency on extensive labeled datasets, offering a pathway to more robust and scalable solutions. In this work, we propose to leverage these advancements to improve the reconstruction of reflective objects from monocular images.

## 3. Method

### 3.1. Preliminary: 2D Gaussian Splatting

Since we focus on achieving high-quality reconstruction, our method builds upon the state-of-the-art surfel-based 2DGS [20] due to its superior geometry performance and efficiency. 2DGS proposes to collapse the 3D volume into a set of 2D-oriented planar Gaussian disks and introduces a perspective-accurate 2D splatting process. Similar to 3DGS, the 2D splat is characterized by its central point  $p_k$ , two principal tangential vectors  $t_u$  and  $t_v$ , and a corresponding scaling vector  $S = (s_u, s_v)$  that controls the variances of the 2D Gaussian distribution. Compared to 3DGS, 2DGS represents the scene’s geometry better because the oriented planar Gaussian can be perfectly aligned to the surface and the normal direction is well-defined as the normal of the plane.

To be specific, a 2D Gaussian disk is defined in a local

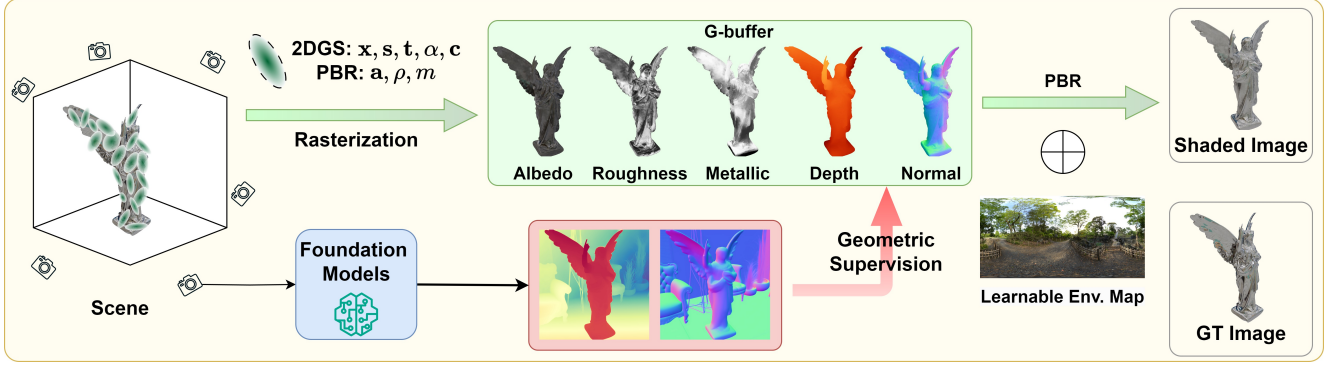


Figure 1. The overview of our GS-2DSG method for reflective object reconstruction. The foundation models supervise 2DGS reconstruction via estimated depth and normal maps to improve geometry and surface smoothness. An environment map is also learned and rendered to account for reflections.

tangent space in world space, parameterized as:

$$P(u, v) = \mathbf{x} + s_u \mathbf{t}_u u + s_v \mathbf{t}_v v \quad (1)$$

And for the point  $\mathbf{u}(u, v)$  in the  $uv$  space, its 2D Gaussian value can then be calculated by standard Gaussian

$$\mathcal{G}(\mathbf{u}) = \exp\left(-\frac{u^2 + v^2}{2}\right) \quad (2)$$

The center  $\mathbf{x}$ , scaling  $(s_u, s_v)$ , and the rotation  $(\mathbf{t}_u, \mathbf{t}_v)$  are learnable parameters. Following 3DGS [26], each 2D Gaussian primitive has opacity  $\alpha$  and view-dependent appearance  $\mathbf{c}$  parameterized with spherical harmonics.

Instead of projecting the 2D Gaussian primitives onto the image space for rendering, 2DGS derives the intersection point of ray and splat in the local tangent space by plane intersection, which alleviates the problem of splat degeneration, especially at grazing angle. The rasterization process is similar to 3DGS, in that 2D Gaussians are sorted based on the depth of their center, and volumetric alpha blending is used to integrate alpha-weighted appearance from front to back:

$$\mathbf{c}(\mathbf{x}) = \sum_{i=1} \mathbf{c}_i \alpha_i \hat{\mathcal{G}}_i(\mathbf{u}(\mathbf{x})) \prod_{j=1}^{i-1} (1 - \alpha_j \hat{\mathcal{G}}_j(\mathbf{u}(\mathbf{x}))) \quad (3)$$

where  $\hat{\mathcal{G}}$  is the object-space low-pass filter introduced in [4]. Please refer to the original paper for more details.

### 3.2. Geometric properties from Gaussian

To reconstruct the surface of the object and utilize the geometric information from the foundation models, we derive the depth and normal rendering from the 2D Gaussian primitives.

**Normal** Different from other 3DGS-based methods [7, 8] that assume the direction of the axis with a minimum scale

factor as the normal direction, the 2D Gaussian primitives in 2DGS have a well-defined normal direction as the normal of the plane. The normal of each 2D Gaussian primitive can be calculated by the cross product of the two principal tangential vectors:

$$\mathbf{n} = \mathbf{t}_u \times \mathbf{t}_v \quad (4)$$

and the normal vector of a point  $\mathbf{x}$  in the screen space can be rendered similar to the color in Eq. (3) as:

$$\hat{N}(\mathbf{x}) = \sum_{i \in M} \mathbf{n}_i \alpha_i \prod_{j=1}^{i-1} (1 - \alpha_j) \quad (5)$$

We omit the low-pass filter  $\hat{\mathcal{G}}$  here and in the following equations for simplicity.

**Depth** For the depth, we follow 2DGS to render the expected depth from the depth by intersections of Gaussians and ray by:

$$D(\mathbf{x}) = \sum_{i \in M} d_i \alpha_i \prod_{j=1}^{i-1} (1 - \alpha_j) / \sum_{i \in M} \alpha_i \prod_{j=1}^{i-1} (1 - \alpha_j) \quad (6)$$

### 3.3. Supervision from Foundation Models

As we discussed in the introduction, the monocular depth and normal estimation models infer the geometric information from a single image based on the knowledge of massive training data. Thus, they are insusceptible to the reflective surface problem. We use the such models [3, 34] to predict normal  $\tilde{N}$  and depth  $\tilde{D}$  for each image. As shown in Fig. 2, the foundation models can produce faithful predictions for the object with different materials.

We use the predicted normal  $\tilde{N}_i$  and depth  $\tilde{D}_i$  as pseudo ground-truth for additional supervision. To be specific, we

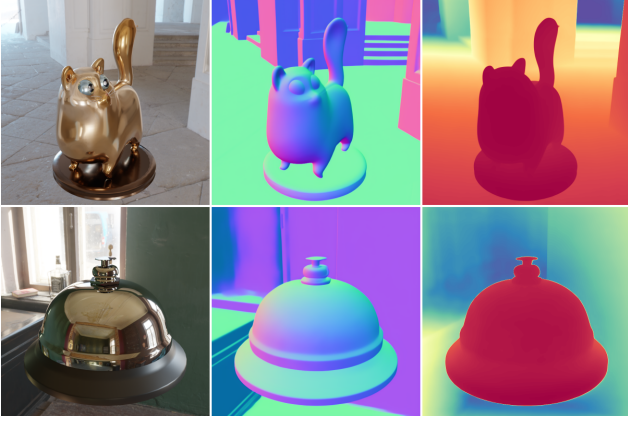


Figure 2. Quality of the normal and depth predictions from the Marigold [25, 34] and Depth Pro [3] foundation models.

supervise the rendered normal map with  $L_1$  and cosine loss by:

$$\mathcal{L}_n = \left\| \hat{N}_i - \tilde{N}_i \right\|_1 + \left( 1 - \hat{N}^T \tilde{N} \right) \quad (7)$$

As for the depth supervision, we adapt the scale-invariant depth loss [37] to supervise the rendered depth map by:

$$\mathcal{L}_d = \left\| (\omega \hat{D} + b) - \tilde{D} \right\|^2 \quad (8)$$

where  $\omega$  and  $b$  are the scale and shift used to align the rendered depth  $\hat{D}$  and the predicted depth  $\tilde{D}$ . We solve for the  $\omega$  and  $b$  by a least-square optimization according to [37].

### 3.4. Shading the Gaussians

#### 3.4.1. Recap on Rendering Equation

In the original Gaussian Splatting, the color of each Gaussian primitive is represented by a view-dependent appearance  $\mathbf{c}$  parameterized with spherical harmonics. However, the appearance of the reflective surface is not well described by the spherical harmonics. Following previous work [18, 22, 31], we introduce physical-based rendering (PBR) pipeline by leveraging the classic rendering equation [23] to formulate the radiance at a viewing direction  $\omega_o$  of a point  $\mathbf{x}$  as:

$$L_o(\mathbf{x}, \omega_o, \mathbf{n}) = \int_{\Omega} f_r(\mathbf{x}, \omega_i, \omega_o) L_i(\mathbf{x}, \omega_i) (\mathbf{n} \cdot \omega_i) d\omega_i \quad (9)$$

where  $\Omega$  denotes the upper hemisphere centered at  $\mathbf{x}$ ,  $\mathbf{n}$  is the normal of the local surface,  $L_i$  is the incoming radiance from the direction  $\omega_i$  and  $f_r$  is the bidirectional reflectance distribution function (BRDF).

From [5], the BRDF  $f_r$  can be divided into diffuse and specular components and further decompose according to

the Cook-Torrance BRDF model [9, 43] as follows:

$$f_r(\omega_i, \omega_o) = \underbrace{(1 - m) \frac{\mathbf{a}}{\pi}}_{\text{diffuse}} + \underbrace{\frac{DFG}{4(\omega_i \cdot \mathbf{n})(\omega_o \cdot \mathbf{n})}}_{\text{specular}} \quad (10)$$

where  $\mathbf{a}$ ,  $m$ ,  $\rho$  are the albedo, metallic, and roughness of the surface respectively,  $D$  is the normal distribution function,  $F$  is the Fresnel term, and  $G$  is the geometry term. The computations of  $D$ ,  $F$  and  $G$  are related to the surface properties and can be found in [43].

According to Eq. (10), the rendering equation Eq. (9) can be rewritten as the sum of the diffuse  $L_d$  and specular  $L_s$  terms:

$L_o(\mathbf{x}, \omega_o, \mathbf{n}) = L_d + L_s$ , where

$$L_d = (1 - m) \frac{\mathbf{a}}{\pi} \int_{\Omega} L_i(\mathbf{x}, \omega_i) (\omega_i \cdot \mathbf{n}) d\omega_i \quad (11)$$

$$L_s = \int_{\Omega} \frac{DFG}{4(\omega_i \cdot \mathbf{n})(\omega_o \cdot \mathbf{n})} L_i(\mathbf{x}, \omega_i) (\omega_i \cdot \mathbf{n}) d\omega_i.$$

We follow [36] to use a trainable High Dynamic Range (HDR) cube map to represent the environment lighting  $L_i(\omega_i)$ . The diffuse term  $L_d$  can be pre-computed and stored as a 2D texture map. As for the specular term  $L_s$ , we employ the *split-sum* approximation [24] to simplify the specular term of the integration.

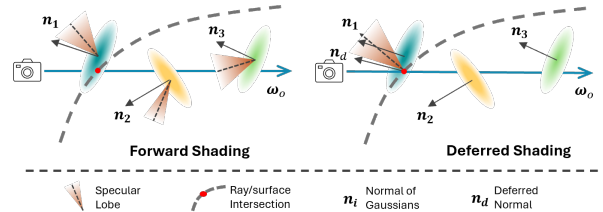


Figure 3. The comparison between forward shading and deferred shading.

### 3.5. Forward Shading vs. Deferred Shading

In order to combine 2D Gaussian primitives with the physical-based rendering (PBR) pipeline, we assign each Gaussian primitive an additional set of PBR parameters ( $\mathbf{a}$ ,  $m$ ,  $\rho$ ). A straightforward approach to render the 2D Gaussian primitives by forward shading, in which we calculate the radiance of each Gaussian  $L_o(\mathbf{x}, \omega_o, \mathbf{n})$  of according to Equation (11), and finally get the accumulated color by alpha-blending as Eq. (3). However, there are several drawbacks: (1) From Eq. (11), the color of a surface point is determined by the shading point position  $\mathbf{x}$ , the normal direction  $\mathbf{n}$ , the viewing direction  $\omega_o$  and the PBR parameters. In the forward shading, as illustrated in Fig. 3, all of the Gaussians along the camera ray will contribute to the accumulated color. This will cause inaccuracy because each

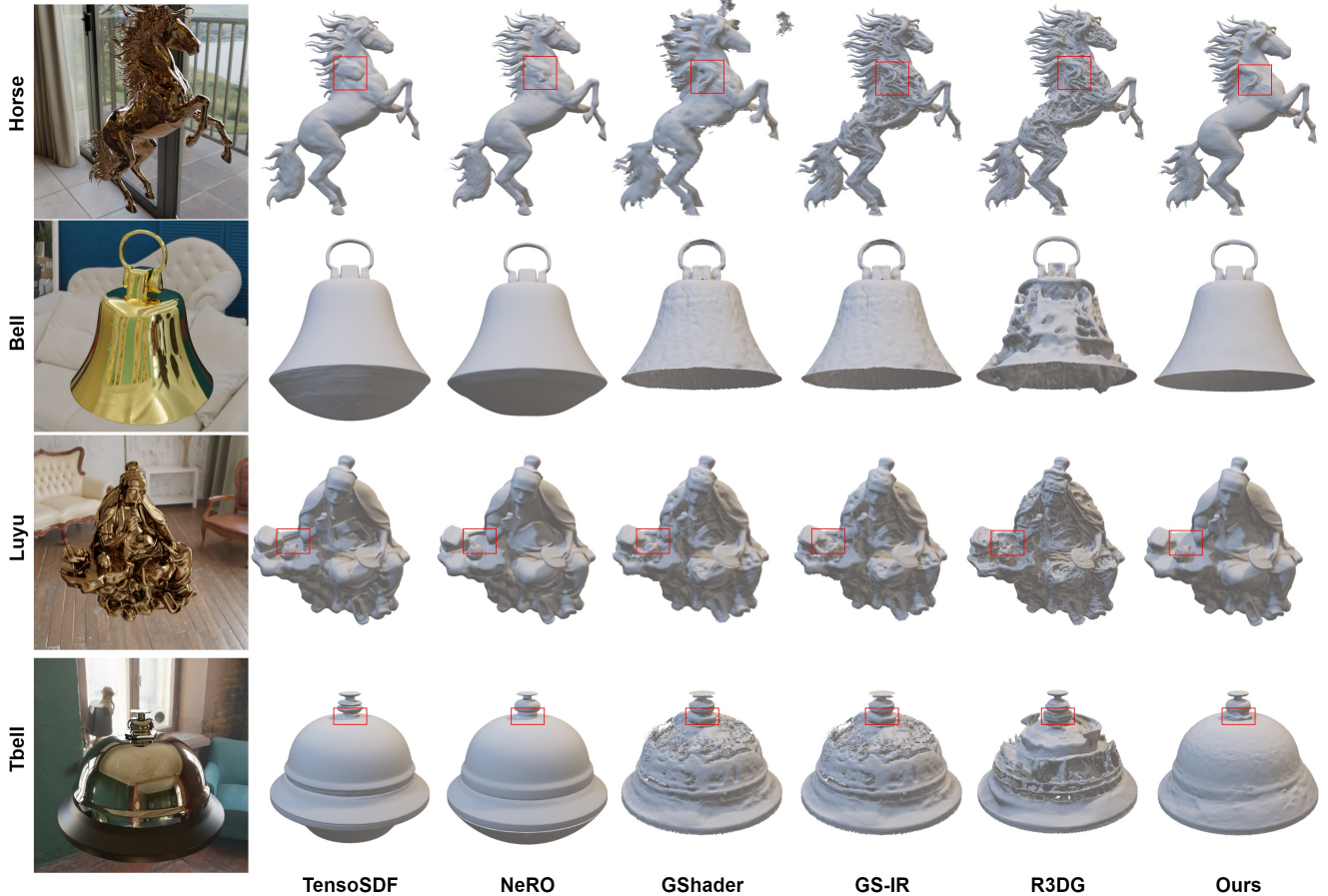


Figure 4. Reconstruction results on the Glossy Bender dataset. Our method achieves significantly better results compared to other Gaussian-based approaches and is comparable to SDF-based methods. We also hold some advantages in finer details than the SDF-based method, as highlighted in the figure.

Gaussian can have a different normal direction, position, and it’s not essential that they are all aligned with the normal of surface. (2) The forward shading is computationally expensive because the shading calculation is performed for each Gaussian primitive.

Based on the above analysis, we decide to adopt the deferred shading technique to render the Gaussians. Deferred shading [11] is a rendering technique that decouples the shading and lighting calculations from the geometry rendering. It’s firstly introduced to Gaussian Splatting by Ye et al. [47] to improve the rendering quality in the presence of specular reflections. The rendering process is divided into two stages: the geometry rendering and the shading stage. In the geometry rendering stage, we render the depth, normal and PBR parameters of the scene into the G-buffer. In the shading stage, we only shade the ray once based on the G-buffer information. As illustrated in Fig. 3, the deferred shading allows us to shade the ray at the correct shading point and normal direction, producing more accurate shading results.

ing results.

### 3.6. Training Objective

We train our model with multiple loss functions. Firstly, we adapt the basic losses  $\mathcal{L}_{GS}$  from 2DGS [20] including RGB reconstruction loss and normal consistency loss. We also introduce the geometric losses  $\mathcal{L}_n$  and  $\mathcal{L}_d$  from the foundation models as we proposed in Sec. 3.3.

Finally, we introduce regularization terms on the lighting and PBR parameters to facilitate the training process. We adapt the natural light regularization from [32] by:

$$\mathcal{L}_{light} = \|\mathbf{L} - \bar{\mathbf{L}}\|^2 \quad (12)$$

where  $\mathbf{L}$  is the predicted environment lighting and  $\bar{\mathbf{L}}$  is the mean of three channels. We also introduce the regularization on the PBR parameters from [18] assuming those properties will not change dramatically in the region of smooth color:

$$\mathcal{L}_{pbr} = \|\nabla \mathbf{X}\| \exp(-\|\nabla \mathbf{C}_{gt}\|) \quad (13)$$

	SDF-based		GShader	Gaussian-based		Ours
	TensoSDF	NERO		GS-IR	R3DG	
Angel	0.0038	0.0034	0.0060	0.0110	0.0090	0.0061
Bell	0.0066	0.0032	0.0078	0.1097	0.0403	0.0037
Cat	0.0267	0.0044	0.0175	0.0566	0.0326	0.0074
Horse	0.0033	0.0049	0.0072	0.0149	0.0117	0.0050
Luyu	0.0083	0.0054	0.0101	0.0224	0.0151	0.0076
Potion	0.0064	0.0053	0.0382	0.0593	0.0380	0.0088
Tbell	0.0212	0.0035	0.0308	0.0989	0.0472	0.0078
Teapot	0.0085	0.0037	0.0178	0.0693	0.0488	0.0083
Average	0.0106	0.0042	0.0169	0.0553	0.0303	0.0068
Training Time (h)	6	12	0.5	0.5	1	0.7

Table 1. The Chamfer- $\mathcal{L}_1 \downarrow$  distance of 3D reconstruction results on the Blender Glossy dataset. We color each cell as **best**, **second**, and **third**. Our method achieves top results among GS-based approaches at similar computational cost, and second best for SDF-based approaches at an order of magnitude less computational cost.

where  $\mathbf{X}$  is the rendered map of PBR parameters similar to Eq. (3) and  $\mathbf{C}_{gt}$  is the ground-truth color.

In total, the final loss function is formulated as a combination of all the losses:

$$\mathcal{L} = \mathcal{L}_{GS} + \lambda_n \mathcal{L}_n + \lambda_d \mathcal{L}_d + \lambda_{light} \mathcal{L}_{light} + \lambda_{pbr} \mathcal{L}_{pbr} \quad (14)$$

## 4. Experiments

Methods	Gshader	GS-IR	R3DG	Ours
Baking	0.0056	0.0064	0.0041	0.0031
Ball	0.0046	0.0249	0.0046	0.0028
Blocks	0.0082	0.0078	0.0064	0.0041
Cactus	0.0074	0.0070	0.0043	0.0039
Car	0.0062	0.0060	0.0045	0.0041
Chips	0.0055	0.0078	0.0044	0.0036
Cup	0.0127	0.0138	0.0108	0.0092
Curry	0.0053	0.0067	0.0040	0.0031
Gnome	0.0067	0.0140	0.0048	0.0041
Grogu	0.0151	0.0149	0.0127	0.0105
Pepsi	0.0065	0.0235	0.0107	0.0035
Pitcher	0.0062	0.0307	0.0186	0.0072
Salt	0.0078	0.0249	0.0044	0.0038
Teapot	0.0056	0.0054	0.0039	0.0031
Average	0.0074	0.0139	0.0070	0.0047

Table 2. The reconstruction quality in terms of the Chamfer- $\mathcal{L}_1 \downarrow$  distance on the Stanford-ORB dataset.

**Datasets.** We conduct experiments on one synthetic dataset Glossy Blender dataset from NeRO [32] and one real-world dataset StanfordORB [27]. The Glossy Blender

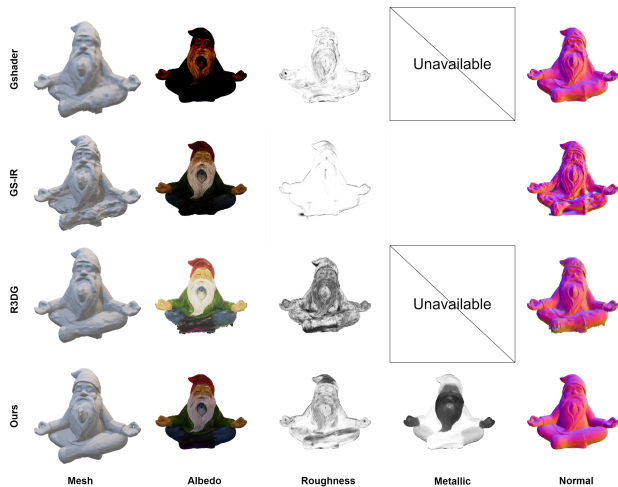


Figure 5. Comparison of the results on the StanfordORB dataset. We show the reconstructed mesh, rendered PBR parameters, and the normal map. Gshader and R3DG do not have Metallic results.

dataset contains 8 objects with highly specular materials, we use it to evaluate the reconstruction and relighting quality. The StanfordORB dataset contains 14 objects with various materials and each object is captured under 3 different lighting conditions. We randomly select one lighting condition from each object. We use the low dynamic range (LDR) images and downsample to  $1024 \times 1024$  for training.

**Implementation Details.** We adopt the Marigold [25] fine-tuned by [34] for normal estimation and Depth Pro [3] for depth estimation for its superior performance on the object level prediction. To stabilize the training, we separate the training process into two stages. At the initial stage,

Methods	GShader	GS-IR	R3DG	Ours
Angel	15.62 / 0.8041	17.77 / 0.8162	19.55 / 0.8279	19.91 / 0.8510
Bell	15.62 / 0.8316	15.69 / 0.8208	18.71 / 0.8387	18.95 / 0.8652
Cat	14.51 / 0.8914	17.38 / 0.8266	20.22 / 0.8623	21.78 / 0.8793
Horse	19.26 / 0.7982	20.97 / 0.8980	21.25 / 0.9025	22.59 / 0.9190
Luyu	14.41 / 0.7372	18.46 / 0.8053	20.30 / 0.8270	18.82 / 0.8235
Potion	11.35 / 0.7663	15.44 / 0.7601	19.81 / 0.8192	17.88 / 0.8299
Tbell	13.37 / 0.8257	14.42 / 0.7491	16.50 / 0.7977	17.55 / 0.8118
Teapot	15.56 / 0.8108	16.78 / 0.8139	17.22 / 0.8179	18.96 / 0.8659
Average	14.96 / 0.8108	17.11 / 0.8113	19.19 / 0.8366	19.56 / 0.8557
Rendering (FPS)	50	214	1.5	160

Table 3. The relighting quality in terms of PSNR $\uparrow$  and SSIM $\downarrow$  on the Blender Glossy dataset, we report the average metrics of three new environment lights. The comparison shows our method achieves the highest rendering quality and competitive framerate.

we train the original 2DGS model with additional geometric loss  $\mathcal{L}_n$  and  $\mathcal{L}_d$  with  $\lambda_n = 0.5$  and  $\lambda_d = 0.05$  for 30000 iterations. We follow use the same as 2DGS for other settings. In the second stage, we enable the PBR pipeline and optimize the geometry, PBR parameters and environment lighting together. The weights for the losses are set as  $\lambda_{\text{light}} = 0.002$ ,  $\lambda_a = 0.05$ ,  $\lambda_m = 0.05$ , and  $\lambda_r = 0.01$ . The second stage takes another 10000 steps to optimize. We implement our method using PyTorch and conduct all the experiments on a single NVIDIA RTX 4090 GPU.

**Baselines and metrics.** For baselines, we select the state-of-the-art methods in the field of reflective object reconstruction and relighting. We compare our method with the following baselines: **SDF-based methods**, NeRO [32]: a method based on NeuS [44] and incorporating PBR pipeline, TensoSDF [28]: based on NeRO with tensorial representation and roughness-aware training objectives. **Gaussian-based methods**, GShader [22]: a method based on 3DGS and incorporating PBR pipeline, GS-IR [31]: a method improving rendering quality by introducing occlusion and illumination baking, R3DG [18]: a method further improves relighting quality by point-based ray-tracing. We evaluate the reconstruction quality using the Chamfer distance and the relighting quality using the PSNR and SSIM metrics.

#### 4.1. Comparison on Reconstruction Quality

We evaluate the reconstruction quality of our method on the Glossy Bender dataset [32] and the StanfordORB dataset [27]. On the Glossy Blender dataset, as shown in Tab. 1, our method achieves the best reconstruction quality among all the Gaussian-based methods. Compared to the SDF-based method, we achieve comparable results with NeRO [32] and better than TensoSDF [28]. The qualitative comparisons are shown in Fig. 4. Compared to Gaussian-

based methods, our method achieves much better reconstruction quality while others are noisy and bumpy. The SDF-based methods generally result in smoother surfaces than ours due to the intrinsic smoothness prior of MLP. Our result is not as smooth as theirs, because there is no such constraint from Gaussian. Our method can capture the fine details of the surface such as the horse’s mane region and the table bell plunger. We also notice the SDF-based methods tend to produce raised surfaces in the unseen region (bottom of the bells) due to the watertight restriction of SDF and the over-smoothing effect while our method gets clean results in those regions.

As for the results on the StanfordORB dataset shown in Tab. 2, we achieve the best reconstruction quality all over the dataset and our method outperforms other baselines in most cases. From the comparison shown in Fig. 5, our method produce reasonable decomposition of the PBR parameters with less noise.

#### 4.2. Relighting Comparison

We further evaluate the relighting quality of our method on the Glossy Bender dataset [32], as presented in Tab. 3. Our method achieves the highest relighting quality among all Gaussian-based methods. Our approach achieves the highest relighting quality among all Gaussian-based methods. The qualitative comparisons in Fig. 6 further illustrate that, leveraging the PBR parameters and geometry from our method, we achieve compelling relighting effects, whereas other methods fail to produce reasonable results.

#### 4.3. Ablation Study

We validate the effectiveness of each component in our method by conducting ablation studies on the Glossy Bender dataset [32] shown in Tab. 4. Starting from the baseline method 2DGS [20], we add the geometric supervision from foundation models. The reconstruction quality is improved significantly with the additional supervision. However the



Figure 6. Relighting results on the Glossy Bender dataset.

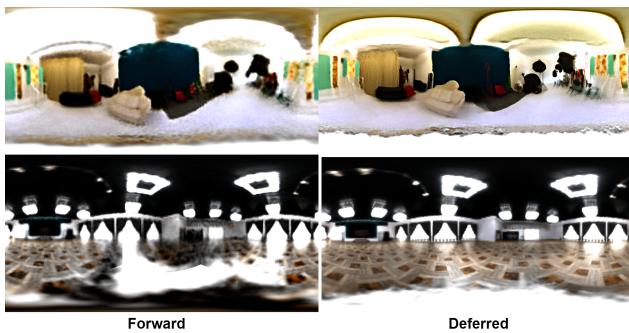


Figure 7. Comparison of environment lighting estimation quality between the deferred shading and forward shading.

rendering quality drops due to the lack of flexibility. We then add the PBR to model the reflective effect, achieving improvement in terms of both reconstruction and rendering quality.

Finally, we add the deferred shading forming the full model. As we analyze in Sec. 3.5, the deferred shading provides more accurate shading components and thus improves the environment lighting estimation. We visualize the estimated environment lighting in Fig. 7. The deferred shading provides a more accurate estimation of the environmental lighting, which leads to better rendering quality.

## 5. Conclusion

In this paper, we introduce GS-2DGS, a Gaussian-based reconstruction method designed specifically for reflective objects. By incorporating a physics-based rendering pipeline, our model captures the interaction between surfaces and en-

2DGS	Geo	PBR	DS	$C-\mathcal{L}_1 \downarrow$	PSNR $\uparrow$
✓				0.0481	26.23
✓	✓			0.0084	25.52
✓	✓	✓		0.0074	25.86
✓	✓	✓	✓	0.0068	26.76

Table 4. Ablation study results on the Glossy Bender dataset. The result shows that geometric supervision from the foundation model has the most significant impact on the performance of reconstruction and the deferred shading technique helps with rendering quality.

vironmental lighting, effectively mimicking the reflective properties of such objects. Leveraging additional geometric supervision from foundation models and incorporating deferred shading, our method achieves high-quality geometry reconstruction and realistic relighting effects at low computational cost.

Despite these advancements and significantly lower computational costs, our method still shows a slight performance gap compared to state-of-the-art SDF-based approaches. We attribute this to the inherent lack of geometric constraints in Gaussian-based methods. While some concurrent works have explored using SDFs to provide additional geometric supervision, these methods typically suffer from high computational costs. Future works could focus on achieving both speed and accuracy in reconstruction, presenting an exciting avenue for further research.

## References

- [1] Gwangbin Bae and Andrew J Davison. Rethinking inductive biases for surface normal estimation. In *Proceedings of the IEEE/CVF Conference on Computer Vision and Pattern Recognition*, pages 9535–9545, 2024. 2
- [2] Jonathan T Barron, Ben Mildenhall, Matthew Tancik, Peter Hedman, Ricardo Martin-Brualla, and Pratul P Srinivasan. Mip-nerf: A multiscale representation for anti-aliasing neural radiance fields. In *Proceedings of the IEEE/CVF international conference on computer vision*, pages 5855–5864, 2021. 2
- [3] Aleksei Bochkovskii, Amaël Delaunoy, Hugo Germain, Marcel Santos, Yichao Zhou, Stephan R Richter, and Vladlen Koltun. Depth pro: Sharp monocular metric depth in less than a second. *arXiv preprint arXiv:2410.02073*, 2024. 1, 3, 4, 6
- [4] Mario Botsch, Alexander Hornung, Matthias Zwicker, and Leif Kobbelt. High-quality surface splatting on today’s gpus. In *Proceedings Eurographics/IEEE VGTC Symposium Point-Based Graphics, 2005.*, pages 17–141. IEEE, 2005. 3
- [5] Brent Burley and Walt Disney Animation Studios. Physically-based shading at disney. In *Acm Siggraph*, pages 1–7. vol. 2012, 2012. 4
- [6] Danpeng Chen, Hai Li, Weicai Ye, Yifan Wang, Weijian Xie, Shangjin Zhai, Nan Wang, Haomin Liu, Hujun Bao, and Guofeng Zhang. Pgsr: Planar-based gaussian splatting for efficient and high-fidelity surface reconstruction. *arXiv preprint arXiv:2406.06521*, 2024. 2
- [7] Hanlin Chen, Chen Li, and Gim Hee Lee. Neusg: Neural implicit surface reconstruction with 3d gaussian splatting guidance. *arXiv preprint arXiv:2312.00846*, 2023. 3
- [8] Hanlin Chen, Fangyin Wei, Chen Li, Tianxin Huang, Yunsong Wang, and Gim Hee Lee. Vcr-gaus: View consistent depth-normal regularizer for gaussian surface reconstruction. *arXiv preprint arXiv:2406.05774*, 2024. 3
- [9] Robert L Cook and Kenneth E Torrance. A reflectance model for computer graphics. *ACM Siggraph Computer Graphics*, 15(3):307–316, 1981. 4
- [10] Pinxuan Dai, Jiamin Xu, Wenxiang Xie, Xinguo Liu, Huamin Wang, and Weiwei Xu. High-quality surface reconstruction using gaussian surfels. In *ACM SIGGRAPH 2024 Conference Papers*, pages 1–11, 2024. 1
- [11] Michael Deering, Stephanie Winner, Bic Schediwy, Chris Duffy, and Neil Hunt. The triangle processor and normal vector shader: a vlsi system for high performance graphics. *Acm siggraph computer graphics*, 22(4):21–30, 1988. 5
- [12] Yiquan Duan, Xianda Guo, and Zheng Zhu. Diffusiondepth: Diffusion denoising approach for monocular depth estimation. In *European Conference on Computer Vision*, pages 432–449. Springer, 2025. 2
- [13] Ainaz Eftekhari, Alexander Sax, Jitendra Malik, and Amir Zamir. Omnidata: A scalable pipeline for making multi-task mid-level vision datasets from 3d scans. In *Proceedings of the IEEE/CVF International Conference on Computer Vision*, pages 10786–10796, 2021. 2
- [14] David Eigen and Rob Fergus. Predicting depth, surface normals and semantic labels with a common multi-scale convolutional architecture. In *Proceedings of the IEEE international conference on computer vision*, pages 2650–2658, 2015. 2
- [15] David Eigen, Christian Puhrsch, and Rob Fergus. Depth map prediction from a single image using a multi-scale deep network. *Advances in neural information processing systems*, 27, 2014. 2
- [16] Xiao Fu, Wei Yin, Mu Hu, Kaixuan Wang, Yuexin Ma, Ping Tan, Shaojie Shen, Dahua Lin, and Xiaoxiao Long. Geowizard: Unleashing the diffusion priors for 3d geometry estimation from a single image. In *European Conference on Computer Vision*, pages 241–258. Springer, 2025. 1
- [17] Chen Gao, Yipeng Wang, Changil Kim, Jia-Bin Huang, and Johannes Kopf. Planar reflection-aware neural radiance fields. *arXiv preprint arXiv:2411.04984*, 2024. 2
- [18] Jian Gao, Chun Gu, Youtian Lin, Hao Zhu, Xun Cao, Li Zhang, and Yao Yao. Relightable 3d gaussian: Real-time point cloud relighting with brdf decomposition and ray tracing. *arXiv preprint arXiv:2311.16043*, 2023. 1, 2, 4, 5, 7
- [19] Yuan-Chen Guo, Di Kang, Linchao Bao, Yu He, and Song-Hai Zhang. Nerfren: Neural radiance fields with reflections. In *Proceedings of the IEEE/CVF Conference on Computer Vision and Pattern Recognition*, pages 18409–18418, 2022. 2
- [20] Binbin Huang, Zehao Yu, Anpei Chen, Andreas Geiger, and Shenghua Gao. 2d gaussian splatting for geometrically accurate radiance fields. In *ACM SIGGRAPH 2024 Conference Papers*, pages 1–11, 2024. 1, 2, 5, 7
- [21] Ivo Ihrke, Kiriakos N Kutulakos, Hendrik PA Lensch, Marcus Magnor, and Wolfgang Heidrich. Transparent and specular object reconstruction. In *Computer graphics forum*, pages 2400–2426. Wiley Online Library, 2010. 2
- [22] Yingwenqi Jiang, Jiadong Tu, Yuan Liu, Xifeng Gao, Xiaoxiao Long, Wenping Wang, and Yuexin Ma. Gaussian-shader: 3d gaussian splatting with shading functions for reflective surfaces. In *Proceedings of the IEEE/CVF Conference on Computer Vision and Pattern Recognition*, pages 5322–5332, 2024. 1, 2, 4, 7
- [23] James T Kajiya. The rendering equation. In *Proceedings of the 13th annual conference on Computer graphics and interactive techniques*, pages 143–150, 1986. 1, 4
- [24] Brian Karis and Epic Games. Real shading in unreal engine 4. *Proc. Physically Based Shading Theory Practice*, 4(3):1, 2013. 4
- [25] Bingxin Ke, Anton Obukhov, Shengyu Huang, Nando Metzger, Rodrigo Caye Daudt, and Konrad Schindler. Repurposing diffusion-based image generators for monocular depth estimation. In *Proceedings of the IEEE/CVF Conference on Computer Vision and Pattern Recognition*, pages 9492–9502, 2024. 1, 4, 6
- [26] Bernhard Kerbl, Georgios Kopanas, Thomas Leimkühler, and George Drettakis. 3d gaussian splatting for real-time radiance field rendering. *ACM Trans. Graph.*, 42(4):139–1, 2023. 1, 2, 3
- [27] Zhengfei Kuang, Yunzhi Zhang, Hong-Xing Yu, Samir Agarwala, Elliott Wu, Jiajun Wu, et al. Stanford-orb: a real-world 3d object inverse rendering benchmark. *Advances in Neural Information Processing Systems*, 36, 2024. 6, 7

- [28] Jia Li, Lu Wang, Lei Zhang, and Beibei Wang. Tensosdf: Roughness-aware tensorial representation for robust geometry and material reconstruction. *ACM Transactions on Graphics (TOG)*, 43(4):1–13, 2024. 1, 2, 7
- [29] Zhengqi Li and Noah Snavely. Megadepth: Learning single-view depth prediction from internet photos. In *Proceedings of the IEEE conference on computer vision and pattern recognition*, pages 2041–2050, 2018. 2
- [30] Zhaoshuo Li, Thomas Müller, Alex Evans, Russell H Taylor, Mathias Unberath, Ming-Yu Liu, and Chen-Hsuan Lin. Neuralangelo: High-fidelity neural surface reconstruction. In *Proceedings of the IEEE/CVF Conference on Computer Vision and Pattern Recognition*, pages 8456–8465, 2023. 2
- [31] Zhihao Liang, Qi Zhang, Ying Feng, Ying Shan, and Kui Jia. Gs-ir: 3d gaussian splatting for inverse rendering. In *Proceedings of the IEEE/CVF Conference on Computer Vision and Pattern Recognition*, pages 21644–21653, 2024. 1, 2, 4, 7
- [32] Yuan Liu, Peng Wang, Cheng Lin, Xiaoxiao Long, Jiepeng Wang, Lingjie Liu, Taku Komura, and Wenping Wang. Nero: Neural geometry and brdf reconstruction of reflective objects from multiview images. *ACM Transactions on Graphics (TOG)*, 42(4):1–22, 2023. 1, 2, 5, 6, 7
- [33] Yifan Mao, Jian Liu, and Xianming Liu. Stealing stable diffusion prior for robust monocular depth estimation. *arXiv preprint arXiv:2403.05056*, 2024. 2
- [34] Gonzalo Martin Garcia, Karim Abou Zeid, Christian Schmidt, Daan de Geus, Alexander Hermans, and Bastian Leibe. Fine-tuning image-conditional diffusion models is easier than you think. In *Proceedings of the IEEE/CVF Winter Conference on Applications of Computer Vision (WACV)*, 2025. 1, 3, 4, 6
- [35] Ben Mildenhall, Pratul P Srinivasan, Matthew Tancik, Jonathan T Barron, Ravi Ramamoorthi, and Ren Ng. Nerf: Representing scenes as neural radiance fields for view synthesis. *Communications of the ACM*, 65(1):99–106, 2021. 2
- [36] Jacob Munkberg, Jon Hasselgren, Tianchang Shen, Jun Gao, Wenzheng Chen, Alex Evans, Thomas Müller, and Sanja Fidler. Extracting triangular 3d models, materials, and lighting from images. In *Proceedings of the IEEE/CVF Conference on Computer Vision and Pattern Recognition*, pages 8280–8290, 2022. 4
- [37] René Ranftl, Katrin Lasinger, David Hafner, Konrad Schindler, and Vladlen Koltun. Towards robust monocular depth estimation: Mixing datasets for zero-shot cross-dataset transfer. *IEEE transactions on pattern analysis and machine intelligence*, 44(3):1623–1637, 2020. 2, 4
- [38] René Ranftl, Alexey Bochkovskiy, and Vladlen Koltun. Vision transformers for dense prediction. In *Proceedings of the IEEE/CVF international conference on computer vision*, pages 12179–12188, 2021. 2
- [39] Ashutosh Saxena, Min Sun, and Andrew Y Ng. Make3d: Learning 3d scene structure from a single still image. *IEEE transactions on pattern analysis and machine intelligence*, 31(5):824–840, 2008. 2
- [40] Saurabh Saxena, Charles Herrmann, Junhwa Hur, Abhishek Kar, Mohammad Norouzi, Deqing Sun, and David J Fleet. The surprising effectiveness of diffusion models for optical flow and monocular depth estimation. *Advances in Neural Information Processing Systems*, 36, 2024. 2
- [41] Jinguang Tong, Sundaram Muthu, Fahira Afzal Maken, Chuong Nguyen, and Hongdong Li. Seeing through the glass: Neural 3d reconstruction of object inside a transparent container. In *Proceedings of the IEEE/CVF Conference on Computer Vision and Pattern Recognition*, pages 12555–12564, 2023. 2
- [42] Dor Verbin, Peter Hedman, Ben Mildenhall, Todd Zickler, Jonathan T Barron, and Pratul P Srinivasan. Ref-nerf: Structured view-dependent appearance for neural radiance fields. In *2022 IEEE/CVF Conference on Computer Vision and Pattern Recognition (CVPR)*, pages 5481–5490. IEEE, 2022. 2
- [43] Bruce Walter, Stephen R Marschner, Hongsong Li, and Kenneth E Torrance. Microfacet models for refraction through rough surfaces. *Rendering techniques*, 2007:18th, 2007. 4
- [44] Peng Wang, Lingjie Liu, Yuan Liu, Christian Theobalt, Taku Komura, and Wenping Wang. Neus: Learning neural implicit surfaces by volume rendering for multi-view reconstruction. *Advances in Neural Information Processing Systems*, 34:27171–27183, 2021. 7
- [45] Yiming Wang, Qin Han, Marc Habermann, Kostas Daniilidis, Christian Theobalt, and Lingjie Liu. Neus2: Fast learning of neural implicit surfaces for multi-view reconstruction. In *Proceedings of the IEEE/CVF International Conference on Computer Vision*, pages 3295–3306, 2023. 2
- [46] Guanglei Yang, Hao Tang, Mingli Ding, Nicu Sebe, and Elisa Ricci. Transformer-based attention networks for continuous pixel-wise prediction. In *Proceedings of the IEEE/CVF International Conference on Computer vision*, pages 16269–16279, 2021. 2
- [47] Keyang Ye, Qiming Hou, and Kun Zhou. 3d gaussian splatting with deferred reflection. In *ACM SIGGRAPH 2024 Conference Papers*, pages 1–10, 2024. 5
- [48] Zhichao Yin and Jianping Shi. Geonet: Unsupervised learning of dense depth, optical flow and camera pose. In *Proceedings of the IEEE conference on computer vision and pattern recognition*, pages 1983–1992, 2018. 2
- [49] Alex Yu, Ruilong Li, Matthew Tancik, Hao Li, Ren Ng, and Angjoo Kanazawa. Plenotrees for real-time rendering of neural radiance fields. In *Proceedings of the IEEE/CVF International Conference on Computer Vision*, pages 5752–5761, 2021. 2
- [50] Mulin Yu, Tao Lu, Linning Xu, Lihan Jiang, Yuanbo Xiangli, and Bo Dai. Gsdf: 3dgs meets sdf for improved rendering and reconstruction. *arXiv preprint arXiv:2403.16964*, 2024. 1, 2
- [51] Chaoqiang Zhao, Youmin Zhang, Matteo Poggi, Fabio Tosi, Xianda Guo, Zheng Zhu, Guan Huang, Yang Tang, and Stefano Mattoccia. Monovit: Self-supervised monocular depth estimation with a vision transformer. In *2022 international conference on 3D vision (3DV)*, pages 668–678. IEEE, 2022. 2
- [52] Wenliang Zhao, Yongming Rao, Zuyan Liu, Benlin Liu, Jie Zhou, and Jiwen Lu. Unleashing text-to-image diffusion models for visual perception. In *Proceedings of the*

*IEEE/CVF International Conference on Computer Vision*, pages 5729–5739, 2023. [2](#)

- [53] Yang Katie Zhao, Shang Wu, Jingqun Zhang, Sixu Li, Chaojian Li, and Yingyan Celine Lin. Instant-nerf: Instant on-device neural radiance field training via algorithm-accelerator co-designed near-memory processing. In *2023 60th ACM/IEEE Design Automation Conference (DAC)*, pages 1–6. IEEE, 2023. [2](#)

# GS-2DGS: Geometrically Supervised 2DGS for Reflective Object Reconstruction

## Supplementary Material

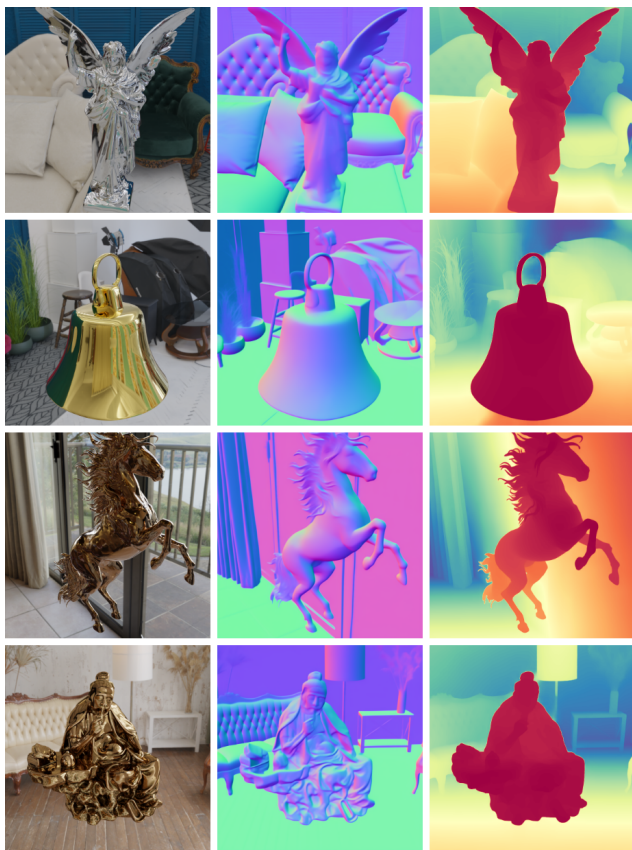


Figure S1. Normal and depth estimation results on the Glossy Blender dataset.

## 1. Additional Implementation Details

### 1.1. Representation

We implement GS-2DGS mainly based on the original 2DGS. The 2DGS uses  $\{\mathbf{x}, \mathbf{s}, \mathbf{t}\}$  and  $\{\alpha, \mathbf{c}\}$  to represent its geometric and volumetric appearance properties respectively, where  $\mathbf{x}$  is the position of the Gaussian,  $\mathbf{s}$  and  $\mathbf{t}$  are the scale and rotation of the axis,  $\alpha$  is the opacity and  $\mathbf{c}$  is the SH coefficients. Apart from those properties, we add PBR parameters  $\{\mathbf{a}, \mathbf{m}, \text{andr}\}$  to represent the albedo, metalness, and roughness of the Gaussian.

### 1.2. Usage of Foundation Models

**Normal Estimation.** We adopt the pre-trained model of Marigold [25] fine-tuned by [34] for normal estimation for its robust performance on the reflective objects. We follow

the original code <sup>1</sup> and default pipeline to use the RGB images as input and predict the normal map.

**Depth Estimation.** For depth estimation, we use the Depth Pro [3] model for its superior performance on the object level prediction. We use the original implementation <sup>2</sup> and follow the original pipeline to predict the depth map. Specially, for the StanfordORB dataset, we use the masked RGB images without the background for better performance.

We show some examples of the normal and depth estimation results in Fig. S1 and Fig. S2.

### 1.3. StanfordORB dataset

Object	Training Scene	Evaluation Scenes
Baking	scene001	scene002, scene003
Ball	scene003	scene002, scene004
Blocks	scene005	scene002, scene006
Cactus	scene001	scene005, scene007
Car	scene004	scene002, scene006
Chips	scene003	scene002, scene004
Cup	scene006	scene003, scene007
Curry	scene001	scene005, scene007
Gnome	scene003	scene005, scene007
Grogu	scene001	scene002, scene003
Pepsi	scene003	scene002, scene004
Pitcher	scene007	scene001, scene005
Salt	scene007	scene004, scene005
Teapot	scene002	scene001, scene006

Table S5. Training and evaluation scenes for each object in the StanfordORB dataset.

The StanfordORB dataset contains 14 objects each in three scenes with different lighting conditions. Both low dynamic range (LDR) and high dynamic range (HDR) images are offered. For each object, we randomly picked one scene for training and the other two for evaluation as illustrated in Tab. S5. The LDR images are downsampled to  $1024 \times 1024$  for training.

<sup>1</sup><https://github.com/VisualComputingInstitute/diffusion-e2e-ft>

<sup>2</sup><https://github.com/apple/ml-depth-pro>

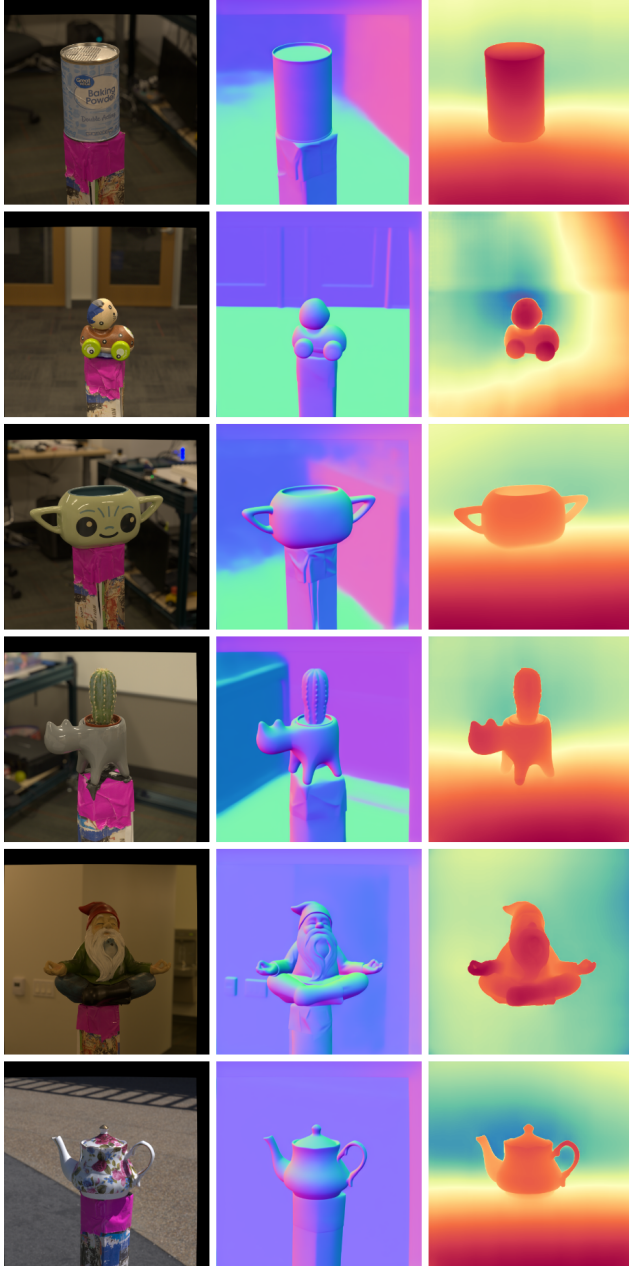


Figure S2. Normal and depth estimation results on the StanfordORB dataset.

## 2. Additional Experiments

### 2.1. Results on Glossy Blender dataset

**Reconstruction** Fig. S3 shows the additional reconstruction results on the Glossy Blender dataset. Our method achieves the best reconstruction quality among all the Gaussian-based methods. Compared to the SDF-based method, we achieve comparable results with NeRO [32] and better than TensoSDF [28]. We also show the normal map

results in Fig. S4.

**Material Decomposition and Relighting.** We show the PBR related material parameters decomposition in Fig. S5 and Fig. S6. We render the corresponding parameter map by alpha blending according to Eq.(3) of the main paper. Compared to other methods, our method can get a more reasonable decomposition of the PBR parameters with less noise. We also show the relighting results of different objects under several environment lights in Fig. S7.

### 2.2. Results on StanfordORB dataset

Here, we provide more details of the experiment results on the StanfordORB dataset.

**Reconstruction** In Fig. S8, we show the comparison of reconstructed geometry among different methods. Our method achieves faithful reconstruction results with less noise and smooth surfaces.

**Material Decomposition and Relighting.** Fig. S9 shows the PBR material decomposition in terms of albedo and roughness. From the results, our method can achieve a more reasonable decomposition of the PBR parameters while GS-IR tends to get high roughness and R3DG’s roughness maps are noisy. We also show the relighting results in Tab. S6 and Fig. S10 to demonstrate the relighting quality further.

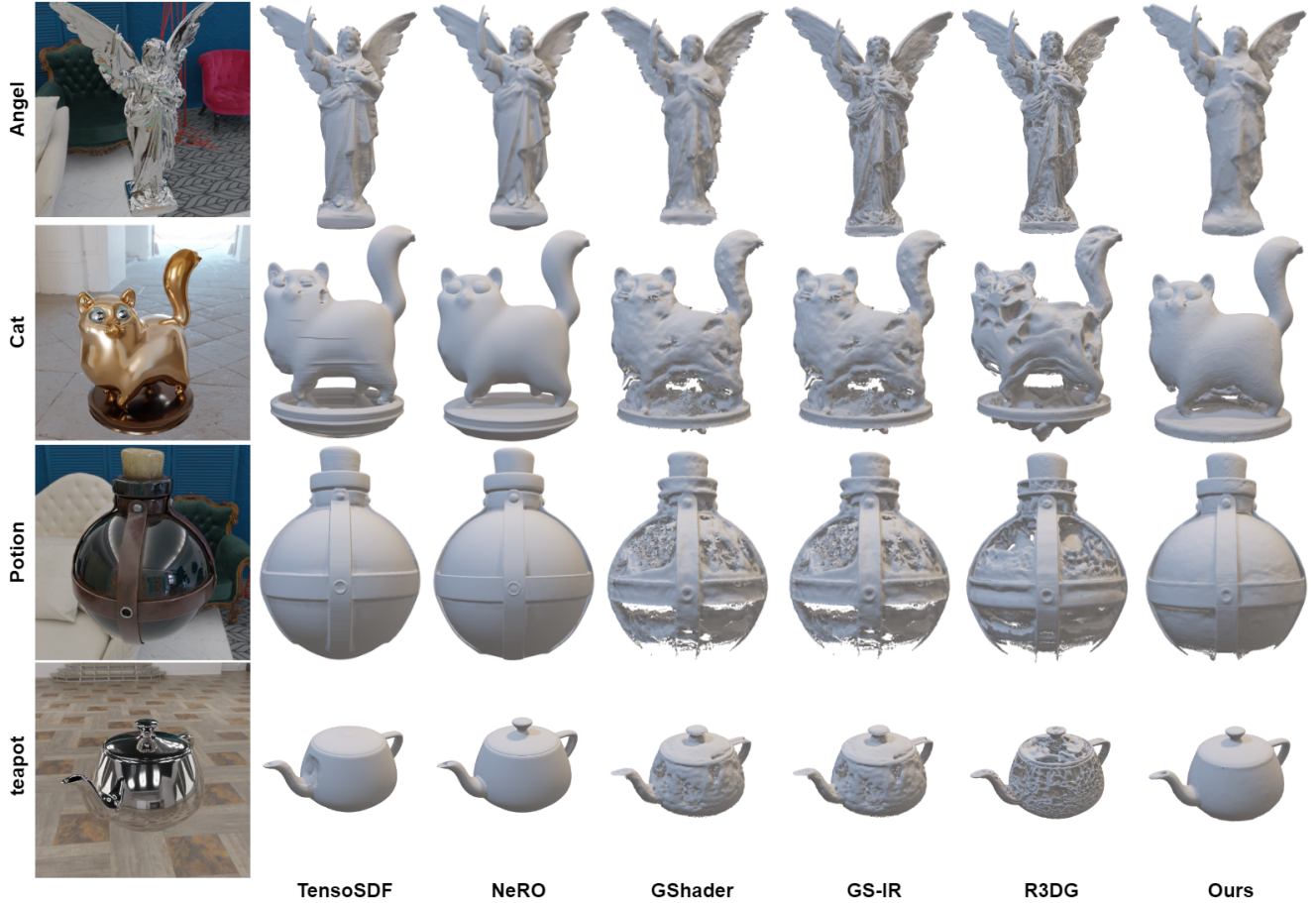


Figure S3. Additional reconstruction results on the Glossy Blender dataset.

Methods	GShader	GS-IR	R3DG	Ours
Baking	23.86 / 0.9586	23.99 / 0.9611	24.71 / 0.9638	24.16 / 0.9593
Ball	22.04 / 0.9219	23.48 / 0.9208	23.19 / 0.9156	25.17 / 0.9357
Blocks	27.09 / 0.9716	28.78 / 0.9707	27.94 / 0.9692	32.16 / 0.9812
Cactus	26.99 / 0.9681	31.94 / 0.9724	30.15 / 0.9650	33.79 / 0.9819
Car	25.13 / 0.9671	26.71 / 0.9670	26.71 / 0.9662	30.57 / 0.9802
Chips	29.94 / 0.9742	28.19 / 0.9673	28.29 / 0.9694	28.36 / 0.9696
Cup	25.90 / 0.9641	26.96 / 0.9592	25.59 / 0.9482	28.93 / 0.9709
Curry	27.37 / 0.9704	30.58 / 0.9666	29.76 / 0.9674	31.77 / 0.9702
Gnome	28.88 / 0.9502	27.92 / 0.9388	26.94 / 0.9254	31.04 / 0.9540
Grogu	25.05 / 0.9709	27.17 / 0.9684	25.17 / 0.9606	25.80 / 0.9737
Pepsi	22.24 / 0.9517	24.46 / 0.9533	22.82 / 0.9490	24.10 / 0.9608
Pitcher	25.55 / 0.9525	27.43 / 0.9545	29.00 / 0.9530	29.53 / 0.9659
Salt	25.64 / 0.9616	23.61 / 0.9289	24.96 / 0.9524	24.74 / 0.9446
Teapot	24.58 / 0.9655	23.86 / 0.9588	23.99 / 0.9575	25.86 / 0.9708
Average	25.73 / 0.9606	26.79 / 0.9563	26.37 / 0.9545	28.28 / 0.9656

Table S6. The relighting quality in terms of PSNR $\uparrow$  and SSIM $\downarrow$  in the StanfordORB dataset, we report the average metrics of two evaluation scenes. The comparison shows our method achieves the highest rendering quality.



Figure S4. Rendered normal maps results on the Glossy Blender dataset.



Figure S5. PBR material parameters decomposition on the Glossy Blender dataset.

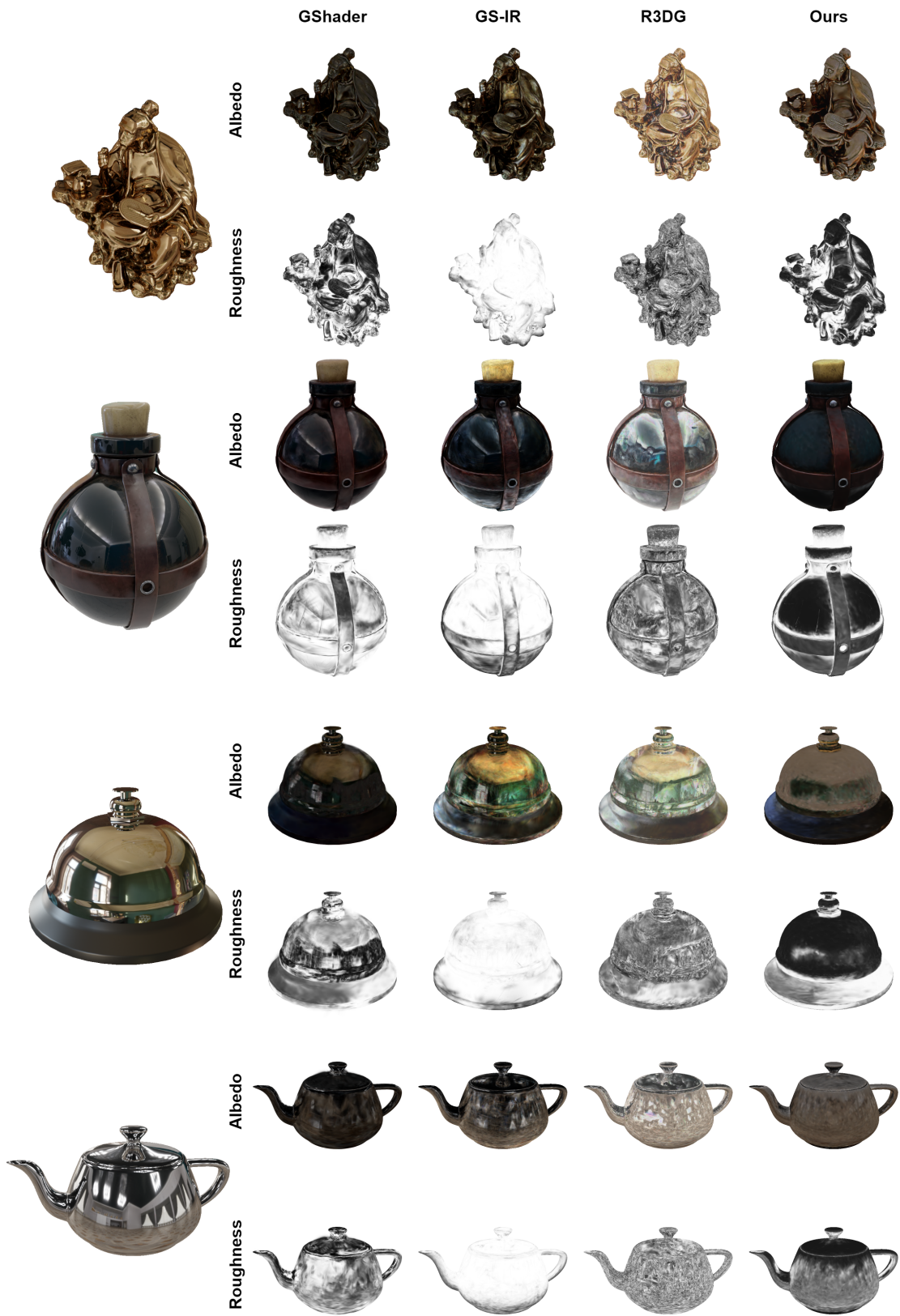


Figure S6. PBR material parameters decomposition on the Glossy Blender dataset.



Figure S7. Relighting results on the Glossy Blender dataset.

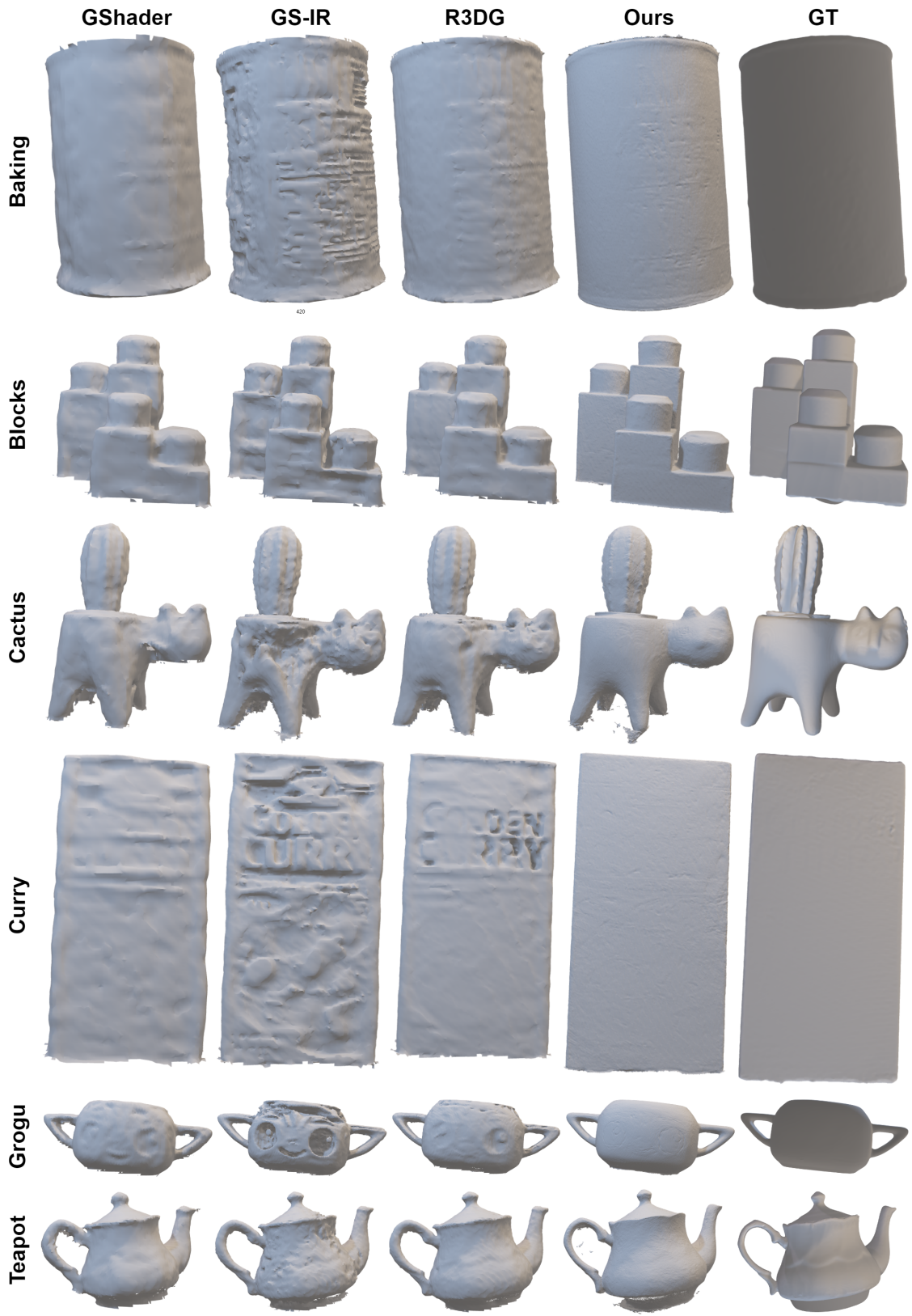


Figure S8. Additional reconstruction results on the StanfordORB dataset.



Figure S9. PBR material decomposition on the StanfordORB dataset.

GShader

GS-IR

R3DG

Ours

GT

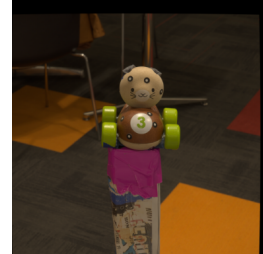


Figure S10. Relighting results on the StanfordORB dataset.